Fitted Hanbury-Brown–Twiss radii versus space-time variances in flow-dominated models

Evan Frodermann, Ulrich Heinz, and Michael Annan Lisa*
Physics Department, The Ohio State University, Columbus, Ohio 43210, USA
(Received 9 February 2006; published 24 April 2006)

The inability of otherwise successful dynamical models to reproduce the Hanbury-Brown–Twiss (HBT) radii extracted from two-particle correlations measured at the Relativistic Heavy Ion Collider (RHIC) is known as the RHIC HBT Puzzle. Most comparisons between models and experiment exploit the fact that for Gaussian sources the HBT radii agree with certain combinations of the space-time widths of the source that can be directly computed from the emission function without having to evaluate, at significant expense, the two-particle correlation function. We here study the validity of this approach for realistic emission function models, some of which exhibit significant deviations from simple Gaussian behavior. By Fourier transforming the emission function, we compute the two-particle correlation function, and fit it with a Gaussian to partially mimic the procedure used for measured correlation functions. We describe a novel algorithm to perform this Gaussian fit analytically. We find that for realistic hydrodynamic models the HBT radii extracted from this procedure agree better with the data than the values previously extracted from the space-time widths of the emission function. Although serious discrepancies between the calculated and the measured HBT radii remain, we show that a more apples-to-apples comparison of models with data can play an important role in any eventually successful theoretical description of RHIC HBT data.

DOI: 10.1103/PhysRevC.73.044908 PACS number(s): 25.75.Ld, 25.75.Gz, 24.10.Nz

I. INTRODUCTION

Two-particle intensity interferometry is widely used to characterize the space-time aspects of the freeze-out configuration in relativistic heavy-ion collisions [1]. It is common to condense this information in terms of characteristic length scales of the homogeneity regions [2] from which particles of a given momentum originate.

In this paper we discuss the degree to which homogeneity lengths extracted in quite different ways may be validly compared. Throughout our study, we restrict ourselves to interference effects between identical, noninteracting bosons, resulting from Bose-Einstein statistics. Since final state interactions (e.g., Coulomb effects) affect most interferometry studies, our study may be regarded (1) as a proof-of-principle example that care must be taken to perform apples-to-apples comparisons and (2) as an estimate of the magnitude of the differences for two popular theoretical models.

The homogeneity length scales are extracted in experiments by assuming that the homogeneity region can be approximated by a Gaussian-profile ellipsoid in configuration space, resulting in a Gaussian two-particle momentum correlation function, and performing a semianalytic Gaussian fit to the relative momentum dependence of the measured correlation function (see, e.g., Ref. [1] for details). Following common practice, we will refer in the following to the size parameters obtained from Gaussian fits to the correlation function as "HBT radii."

Fitting experimental data to functional forms other than Gaussian is common in studies of elementary particle collisions, for which Gaussian fits clearly fail. In heavy-ion collisions, the Gaussian ansatz works relatively well, but, especially with the high-quality and high-statistics data sets now available at RHIC, finer, non-Gaussian structures may be physically interesting. Instead of inventing *ad hoc* functional forms with which to fit the correlation functions, or functionally expanding about a Gaussian fitting form [3,4], imaging [5–7] the homogeneity region is perhaps the most promising route to explore these structures. In this paper we do not take up this issue. Instead, we note that most experimental studies in heavy-ion physics to date have used the Gaussian ansatz [1], and we explore some ways in which HBT radii obtained in this way from data may be compared with model calculations.

If the homogeneity region is indeed Gaussian in profile, then the HBT radii agree exactly with appropriate combinations of the root-mean-squared (RMS) variances of its spatial distribution [8]. Given a theoretical model for the freeze-out configuration, calculating these space-time variances is much easier than computing and fitting the correlation function. Many comparisons between models and data therefore use this shortcut, comparing the space-time variances directly with the experimental HBT radii. However, since the homogeneity region is seldom perfectly Gaussian, such direct comparisons are questionable.

This raises the question to what extent some of the persistently observed discrepancies between model predictions and measurements of the HBT radii [1] (the so-called RHIC HBT Puzzle) might be due to such an apples-with-oranges comparison. Indeed, HBT radii calculated with Boltzmann/cascade models that are based on Gaussian fits to the simulated correlation functions agree somewhat better with measurements than do radii based on an extraction of space-time variances from hydrodynamic calculations [1]. Whether this is due to a more realistic modeling of the collision in the Boltzmann/cascade approach or the shortcomings of the comparison of variances with HBT radii in the hydrodynamic case is unclear. Similarly, differences between hydrodynamic

*Electronic address: lisa@mps.ohio-state.edu

calculations of space-time variances [9,10] and Gaussian HBT radii fitted to three-dimensional [11–13] and one-dimensional [14,15] correlations have been observed. However, since these calculations were performed by using different initial conditions and other parameters, it is unclear whether this, or the different extraction methods, were responsible for the observed differences.

Isolating the effect of the method itself is best done by using the same hydrodynamic model and parameters and comparing radii calculated in different ways. One such study [16] compared space-time variances with Gaussian radii extracted from moments of the calculated correlation function. For identical kaon correlations, the radii extracted were almost independent of the method used. In the present study, we use a more sophisticated technique to emulate the three-dimensional Gaussian fits used by experimentalists, and we focus on pion correlations, for which the HBT Puzzle has been studied in detail. In our study, we find that the method used to extract the radii does, indeed, matter.

One cascade model (MPC [17]) that reports RMS variances shows discrepancies with data similar to the hydrodynamic models. Studies [18–20] performed within the Boltzmann/cascade framework show that space-time variances of the freeze-out configuration and Gaussian fits to the correlator can yield quite different radius parameters, due mostly to long tails in the spatial freeze-out distribution from resonance decays that strongly affect the space-time variances but are not reflected in Gaussian fits to the correlation function, according to hydrodynamic calculations [21]. (See, however, the recent study by Kisiel *et al*. [22], which addresses this issue in detail in the context of a blast-wave parametrization.) Hydrodynamic calculations of the space-time variances therefore usually do not include resonance decay contributions in the emission function [9]. Still, the comparison in Ref. [9] involves two differently determined quantities, and in the present paper we eliminate this shortcoming.

To do so requires two additional steps beyond the calculation of the model emission function: (i) The correlation function must be computed via Fourier transformation (for noninteracting identical particles) or by folding with a relative wave function that includes final state interaction effects (for with long-range final state interactions). This is straightforward, albeit numerically expensive since it involves multiple space-time integrals. (ii) A Gaussian fit to the three-dimensional correlation function must be performed, including a correlation strength parameter λ as in the experiment.

We here concentrate on noninteracting pairs of identical particles as the most important case in practice and also in order to simplify as much as possible the computation of the correlator. For the second step we develop an analytical Gaussian fit algorithm that reduces the multidimensional fit problem to a simple set of linear equations for diagonalizing a four-dimensional matrix. This should help theoretical modelers to overcome the barrier of unfamiliarity when faced with a multiparameter fitting problem.

We apply our procedure to emission functions from hydrodynamic calculations [9] and from the blast-wave parametrization [23]. Both generate non-Gaussian freeze-out distributions, due in large measure to finite-size effects coupled with strong collective flow, which is known to be important at RHIC. On the way, we also discuss and analyze Gaussian fits to one-dimensional projections of the three-dimensional correlator. This allows for comparison with earlier work along these lines [14,21] and first introduces our new analytic Gaussian fit algorithm in an easy and transparent simpler setting.

II. VARIANCES VERSUS HBT RADII

Experimentally, the correlation function between two identical particles, as a function of their relative momentum $\boldsymbol{q} \equiv \boldsymbol{p}_a - \boldsymbol{p}_b$ and their average (pair) momentum $\boldsymbol{K} \equiv (\boldsymbol{p}_a + \boldsymbol{p}_b)/2$, is given by

$$C(\boldsymbol{q}, \boldsymbol{K}) = \frac{A(\boldsymbol{q}, \boldsymbol{K})}{B(\boldsymbol{q}, \boldsymbol{K})}, \tag{1}$$

where $A(\boldsymbol{q}, \boldsymbol{K})$ is the signal distribution and $B(\boldsymbol{q}, \boldsymbol{K})$ is the reference or background distribution, which is ideally similar to A in all respects except for the presence of femtoscopic correlations (see, e.g., Ref. [1] for details). $C(\boldsymbol{q}, \boldsymbol{K})$ is the modification of the conditional probability for measuring particle b with momentum $\boldsymbol{p}_b = \boldsymbol{K} - \frac{1}{2}\boldsymbol{q}$ if particle a has been measured with momentum $\boldsymbol{p}_a = \boldsymbol{K} + \frac{1}{2}\boldsymbol{q}$, due to two-particle effects sensitive to space-time separation, too. The explicit $\boldsymbol{K}$ dependence reflects the fact that the separation distribution may depend on the average momentum of the pair [2] and in general does so for exploding sources [24].

Theoretically, the correlation function can be calculated from the emission function $S(\boldsymbol{p}, x)$ describing the probability to emit a particle from space-time point x with momentum $\boldsymbol{p}$, by convoluting it with the two-particle relative wave function [1]. For pairs of noninteracting identical particles one has simply [1,3]

$$C(\boldsymbol{q}, \boldsymbol{K}) \approx 1 + \left| \frac{\int d^4x S(\boldsymbol{K}, x)\, e^{iq\cdot x}}{\int d^4x S(\boldsymbol{K}, x)} \right|^2 . \tag{2}$$

Here $q \cdot x = q^0 t - \boldsymbol{q} \cdot \boldsymbol{x}$, with $q^0 = E_a - E_b = \boldsymbol{\beta} \cdot \boldsymbol{q}$, where $\boldsymbol{\beta} = \boldsymbol{K}/K^0 = 2\boldsymbol{K}/(E_a + E_b)$ is the average velocity of the pair. The $\approx$ sign in Eq. (2) indicates the smoothness approximation, which replaces both $\boldsymbol{p}_a$ and $\boldsymbol{p}_b$ by $\boldsymbol{K}$ inside the emission functions in the denominator [3]. Equation (2) can be decomposed as

$$C(\boldsymbol{q}, \boldsymbol{K}) = 1 + \langle \cos(q \cdot x) \rangle^2 + \langle \sin(q \cdot x) \rangle^2, \tag{3}$$

where $\langle \ldots \rangle$ indicates the ($\boldsymbol{K}$-dependent) space-time average with the emission function:

$$\langle f \rangle \equiv \frac{\int d^4x f(x)\, S(\boldsymbol{K}, x)}{\int d^4x S(\boldsymbol{K}, x)} . \tag{4}$$

If $S(\boldsymbol{K}, x)$ is a four-dimensional *Gaussian* distribution of freeze-out points, the correlation function will likewise be Gaussian in the relative momentum $\boldsymbol{q}$. It takes a particularly simple form for midrapidity pairs (with vanishing longitudinal pair momentum, $K_L = 0$) from central collisions between equal-mass spherical nuclei [1,8]:

$$C(\boldsymbol{q}) = 1 + \lambda e^{-\left(q_o^2 R_o^2 + q_s^2 R_s^2 + q_l^2 R_l^2\right)}. \tag{5}$$

Here q_o, q_s, q_l are the relative momentum components in the Bertsch-Pratt (out-side-long) coordinate system [1,8]. The pair momentum dependence of the correlation function $C(\boldsymbol{q}, \boldsymbol{K})$ leads to $\boldsymbol{K}$ dependencies of the HBT radii R_o, R_s, and R_l (which characterize the relative momentum widths of the correlation function) and of the correlation strength λ. For fully chaotic theoretical Gaussian sources $\lambda \equiv 1$, but for experimental correlation functions usually $\lambda < 1$. Even though we here perform a theoretical model analysis, we keep λ as a parameter because Gaussian fits to non-Gaussian correlation functions generally also yield $\lambda \neq 1$, and experimentally such non-Gaussian effects on the extracted λ cannot be separated from other origins of reduced correlation strength (such as contamination from misidentified particles and contributions from resonance decays [1]). The HBT radii defined by Eq. (5) convey all available geometric information about the source $S(\boldsymbol{K}, x)$.

For Gaussian sources the radius parameters R_o, R_s, and R_l can be calculated directly from the source distribution S as RMS variances. For midrapidity pairs with $K_L = 0$ one finds [8]

$$\begin{aligned} R_o^2 &= \langle \tilde{x}_o^2 \rangle - 2\beta \langle \tilde{x}_o \tilde{t} \rangle + \beta^2 \langle \tilde{t}^2 \rangle, \\ R_s^2 &= \langle \tilde{x}_s^2 \rangle, \qquad R_l^2 = \langle \tilde{x}_l^2 \rangle, \end{aligned} \tag{6}$$

where $\beta = K_T/K^0$ is the magnitude of the (transverse) pair velocity (which points in the x_o direction), and

$$\tilde{x}^\mu \equiv x^\mu - \langle x^\mu \rangle \tag{7}$$

denotes the distance from the ($\boldsymbol{K}$-dependent) center of the homogeneity region for particles with momentum $\boldsymbol{K}$.

Experimentalists commonly extract HBT radii by fitting their experimental correlation functions (1) with the functional form (5). In contrast, most (but not all) theoretical model predictions for HBT radii are based on a calculation of the space-time variances of the emission function and assuming the validity of Eqs. (6), which holds for Gaussian sources. Of course, there is no *a priori* reason to expect a source with a *perfectly* Gaussian profile. Even the simplest flow-dominated freeze-out parametrizations produce clear non-Gaussian tails and edges [23]. On the experimental side, high-statistics measurements show non-Gaussian behavior, which is, however rarely treated quantitatively [4]. In the presence of such non-Gaussian features, the issues are (1) whether the two approaches yield significantly different results and (2) whether either method characterizes the physically interesting length scales of the source sufficiently well. Here, we address the first issue in the context of blast-wave and hydrodynamic models.

Our calculations do not include experimental noise, particle misidentification, or contributions from the decay of long-lived resonances, which can reduce the fit parameter λ in Eq. (5) from its theoretical value of unity [1,21]. Instead, this parameter absorbs (and reflects) some of the effects of fitting a non-Gaussian function to a Gaussian form. This will, of course, also happen in experiment whenever the correlation function deviates from a simple Gaussian. This particular contribution to the fitted correlation strength λ has so far received little attention. The model results presented here should help to assess the possible influence of non-Gaussian features in the data on the fitted values of λ.

III. DIRECT CALCULATION OF HBT RADII

As explained in the Introduction, we here use model emission functions to compute the correlation function according to Eqs. (2) and (3) and then fit the latter with a Gaussian, using a procedure very similar to the one used in experiment. The main difference is that the theoretical correlation function can be calculated with arbitrary precision, so the notion of a statistical error does not enter. Still, we will see that the fitting problem can be formulated in a quite analogous way.

In the following subsection we introduce the algorithm for Gaussian fits through one-dimensional cuts or projections of the three-dimensional correlation function. The full algorithm for three-dimensional Gaussian fits is presented in Sec. III B.

A. One-dimensional Gaussian fits

In Sec. VI of their paper, Wiedemann and Heinz [21] calculated correlators for various model emission functions and extracted parameters from fits to *one-dimensional slices* of the three-dimensional correlation function. Although those authors called them HBT radii, we will call them 1D radii to distinguish them from radii extracted from full three-dimensional fits of the type performed by experimentalists.

In a given direction i ($i = o, s, l$) they calculate the correlator along one of the axes i: $C(q_i; q_{j\neq i} = 0)$. They then find the 1D radius $R^2_{1\mathrm{D},i}$ and the "directional lambda parameter" λ_i that best approximates the correlator according to

$$C(q_i; q_{j\neq i} = 0) \approx 1 + \lambda_i e^{-q_i^2 R^2_{1\mathrm{D},i}}. \tag{8}$$

In particular, they calculated the correlator for a set of N values $q_i^{(k)}$ (similar to experimentally binning the correlation function into N $\boldsymbol{q}$ bins) and minimized numerically the quantity

$$\sum_{k=1}^{N} \left\{ \ln\left[C\left(q_i^{(k)}; q_{j\neq i}^{(k)} = 0\right) - 1\right] - \ln\lambda_i + R^2_{1\mathrm{D},i}\left(q_i^{(k)}\right)^2 \right\}^2. \tag{9}$$

This is reminiscent of the quantity typically minimized by experimenters, although in this case one also takes into account the experimental uncertainty of the measured correlator by weighting each term in the sum (bin) with the inverse experimental error:

$$\chi^2_{1\mathrm{D},i} \equiv \sum_{k=1}^{N} \left\{ \frac{\ln\left[C\left(q_i^{(k)}; q_{j\neq i}^{(k)} = 0\right) - 1\right] - \ln\lambda_i + R^2_{1\mathrm{D},i}\left(q_i^{(k)}\right)^2}{\sigma'^{(k)}_{1\mathrm{D},i}} \right\}^2. \tag{10}$$

Here, $\sigma'^{(k)}_{1\mathrm{D},i}$ represents the uncertainty in bin k in the quantity to be fitted, namely, $\ln[C(q_i^{(k)}; q_{j\neq i}^{(k)} = 0) - 1]$. It is related to the uncertainty $\sigma^{(k)}_{1\mathrm{D},i}$ in the measured correlator $C(q_i^{(k)}; q_{j\neq i}^{(k)} = 0)$

itself by

$$\sigma'^{(k)}_{1\mathrm{D},i} = \frac{d\ln\left[C\left(q_i^{(k)}; q_{j\neq i}^{(k)}=0\right)-1\right]}{dC\left(q_i^{(k)}; q_{j\neq i}^{(k)}=0\right)}\sigma^{(k)}_{1\mathrm{D},i} = \frac{\sigma^{(k)}_{1\mathrm{D},i}}{C\left(q_i^{(k)}; q_{j\neq i}^{(k)}=0\right)-1}. \quad (11)$$

Minimization of quantity (9) as in Ref. [21] is equivalent to setting all uncertainties $\sigma'^{(k)}_{1\mathrm{D},i}$ to the same constant value, independent of k. However, uncertainties in experimental correlation functions typically have approximately constant (k-independent) uncertainties in the bin contents $C(q_i^{(k)}; q_{j\neq i}^{(k)} = 0)$ themselves [25]. Although statistical uncertainties in calculated correlators may in principle be vanishingly small, the weighting factor $[C(q_i^{(k)}; q_{j\neq i}^{(k)}=0)-1]^2$ that appears in Eq. (10) as a result of Eq. (11) will in general affect the resulting fit parameters. We choose to mimic the experimental situation by minimizing Eq. (10), assuming constant (i.e., k-independent) and infinitesimally small errors on C, $\sigma^{(k)}_{1\mathrm{D},i} = \sigma_{1\mathrm{D},i} \to 0$.

Minimizing $\chi^2_{1\mathrm{D},i}$ in Eq. (10) with respect to the fit parameters $\ln\lambda_i$ and $R^2_{1\mathrm{D},i}$ by setting

$$\frac{\partial\chi^2_{1\mathrm{D},i}}{\partial\ln\lambda_i} = 0, \qquad \frac{\partial\chi^2_{1\mathrm{D},i}}{\partial R^2_{1\mathrm{D},i}} = 0, \quad (12)$$

we find after minimal algebra

$$\ln\lambda_i = \frac{X_{2,i}Y_{2,i} - X_{0,i}Y_{4,i}}{Y^2_{2,i} - Y_{0,i}Y_{4,i}}, \quad (13)$$

$$R^2_{1\mathrm{D},i} = \frac{X_{2,i}Y_{0,i} - X_{0,i}Y_{2,i}}{Y^2_{2,i} - Y_{0,i}Y_{4,i}}, \quad (14)$$

where the quantities

$$X_{n,i} = \sum_{k=1}^{N} \frac{\left(q_i^{(k)}\right)^n}{\left(\sigma'^{(k)}_{1\mathrm{D},i}\right)^2}\ln\left[C\left(q_i^{(k)}; q_{j\neq i}^{(k)}=0\right)-1\right], \quad (15)$$

$$Y_{n,i} = \sum_{k=1}^{N} \frac{\left(q_i^{(k)}\right)^n}{\left(\sigma'^{(k)}_{1\mathrm{D},i}\right)^2} \quad (16)$$

are directly calculable from the calculated correlator. Note that the constant error $\sigma_{1\mathrm{D},i}$ of the correlator drops out from the ratios in Eqs. (13) and (14), so the limit $\sigma_{1\mathrm{D},i} \to 0$ mentioned above is well defined.

Minimization of $\chi^2_{1\mathrm{D},i}$ differs significantly from the experimentalists' three-dimensional fits. In particular, it assumes complete factorization of the correlation function in the o, s, l directions. For at least two reasons, this need not be so in reality:

(i) In a full three-dimensional fit, the three directions are coupled by requiring a single λ parameter, independent of direction i. After all, according to Eq. (8) $\lim_{|\boldsymbol{q}|\to 0} C(\boldsymbol{q}) = \lim_{q_i\to 0} C(q_i; q_{j\neq i=0}) = 1+\lambda_i$ should be independent of direction i. Thus, allowing directional lambda parameters may cause the 1D fits to differ significantly from 3D fits.

(ii) Perhaps more important, fitting separately along the q_i axes accounts for only a set of zero measure of the full three-dimensional correlation function. In particular, the correlation function may contain in the exponent terms such as $q_o^2 q_s^2$ or $q_o^4 q_l^2$. (For symmetry reasons [26] odd powers of q_i vanish at midrapidity for central collisions between equal nuclei.) Such higher-order terms will affect the 3D fits of the experimentalist but have no effect on Eq. (10).

We therefore now turn to full three-dimensional Gaussian fits. We will see that the above analytic expressions are easily generalized for this case.

B. Three-dimensional Gaussian fit algorithm

Proceeding as in the previous subsection, we start from the general three-dimensional Gaussian ansatz (5), which can be written as

$$\ln[C(\boldsymbol{q})-1] = \ln\lambda - \left(q_o^2R_o^2 + q_s^2R_s^2 + q_l^2R_l^2\right). \quad (17)$$

If the correlation function $C(\boldsymbol{q}^{(k)})$ in bin k has error σ_k, the error on $\ln(C-1)$ is given as in Eq. (11) by

$$\sigma'_k = \frac{\sigma_k}{C(\boldsymbol{q}^{(k)})-1}. \quad (18)$$

We minimize

$$\chi^2 = \sum_{k=1}^{N}\left\{\frac{\ln\left[C(\boldsymbol{q}^{(k)})-1\right] - \ln\lambda + \sum_{i=osl}\left(q_i^{(k)}\right)^2R_i^2}{\sigma'_k}\right\}^2 \quad (19)$$

by setting

$$\frac{\partial\chi^2}{\partial\ln\lambda} = 0, \qquad \frac{\partial\chi^2}{\partial R_i^2} = 0 \quad (i = o, s, l). \quad (20)$$

This leads to a set of four coupled linear equations,

$$\sum_\beta T_{\alpha\beta}P_\beta = V_\alpha, \quad (21)$$

where α and β take the values $\emptyset, o, s, l$. The vectors appearing here are

$$P = \left(\ln\lambda, R_o^2, R_s^2, R_l^2\right), \quad (22)$$

$$V_\emptyset = -\sum_{k=1}^{N}\frac{\ln\left[C(\boldsymbol{q}^{(k)})-1\right]}{(\sigma'_k)^2}, \quad (23)$$

$$V_i = +\sum_{k=1}^{N}\frac{\left(q_i^{(k)}\right)^2}{(\sigma'_k)^2}\ln\left[C(\boldsymbol{q}^{(k)})-1\right], \quad (24)$$

while the symmetric 4×4 matrix T has components

$$T_{\emptyset\emptyset} = -\sum_{k=1}^{N}\frac{1}{(\sigma'_k)^2}, \qquad T_{\emptyset i} = +\sum_{k=1}^{N}\frac{\left(q_i^{(k)}\right)^2}{(\sigma'_k)^2}, \qquad T_{ij} = -\sum_{k=1}^{N}\frac{\left(q_i^{(k)}\right)^2\left(q_j^{(k)}\right)^2}{(\sigma'_k)^2}. \quad (25)$$

In Equations (24) and (25) $i, j = o, s, l$ as usual. Note the correspondences $V_\alpha \leftrightarrow X_{n,i}$ and $T_{\alpha\beta} \leftrightarrow Y_{n,i}$ between the 3D and 1D cases.

The set of linear equations (21) is easily solved algebraically by diagonalizing the matrix $T_{\alpha\beta}$.

IV. APPLICATION TO BLAST-WAVE MODEL

Many variants of hydrodynamically-inspired models of freeze-out have recently been used to calculate spatial RMS variances that then were compared with experimental HBT radii. A recent example is reported in Ref. [23]. The model itself is very simplistic and ignores, for example, resonance decay contributions that may be important [21]. We ignore such issues with the model itself and simply use it here to discuss differences between RMS variances and Gaussian HBT radii.

We use realistic model parameters that best describe the data [4]. Specifically, we take $R = 13.3$ fm for the source radius, $T = 97$ MeV for the temperature, $\rho_0 = 1.03$ for the maximum transverse flow rapidity, $\tau = 9$ fm/c for the average freeze-out time, and $\Delta\tau = 2.83$ fm/c for the emission duration (see Ref. [23] for details).

A. Correlation functions and analytic fits: results

Equation (12) of Ref. [23] gives the functional form for the single-pion emission function in the blast-wave model. Using this for $S(\boldsymbol{K}, x)$, we calculate the correlation function for pion pairs with longitudinal pair momentum $K_L = 0$, using a Monte Carlo technique to numerically perform the integrals in Eq. (3).

As with experimental data, the correlation function is evaluated in finite-sized three-dimensional bins in (q_o, q_s, q_l) of width 2.5 MeV/c in each direction. One-dimensional slices of the correlation function in the out, side, and long directions are shown in Figs. 1 and 2, for midrapidity pion pairs with $K_T = 0$ and $K_T = 0.3$ GeV/c, respectively.

The slices of the correlation functions appear quite Gaussian, and they are tracked well by the three-dimensional Gaussian fit; the fitted correlation strength λ is very close to 1. The radius parameters calculated from the RMS variances (6) agree quite well with the HBT radii extracted from the three-dimensional Gaussian fit by solving Eqs. (21); both sets are given in the figures. Upon closer inspection one notices, however, that the fitted outward and longitudinal radii, R_o and especially R_l, tend to be systematically smaller than those extracted from the spatial RMS variances; the opposite is true for the sideward radii R_s for which the RMS variances give slightly smaller values than the Gaussian fit. While these differences are small for the blast-wave model parametrization (at least with the realistic parameters studied here), they will be significantly larger (with the same basic tendencies as found here) for the hydrodynamic model source studied in Sec. V.

The Gaussian fit parameters given in Figs. 1 and 2 correspond to using the largest possible $\boldsymbol{q}$ range in the sums over k in Eqs. (24) and (25), discarding only those data points for which C is so close to 1 that the Monte Carlo integration sometimes yields negative values for $C-1$. Due to small but noticeable deviations of the correlation function from a pure Gaussian, the Gaussian fit parameters depend on the number

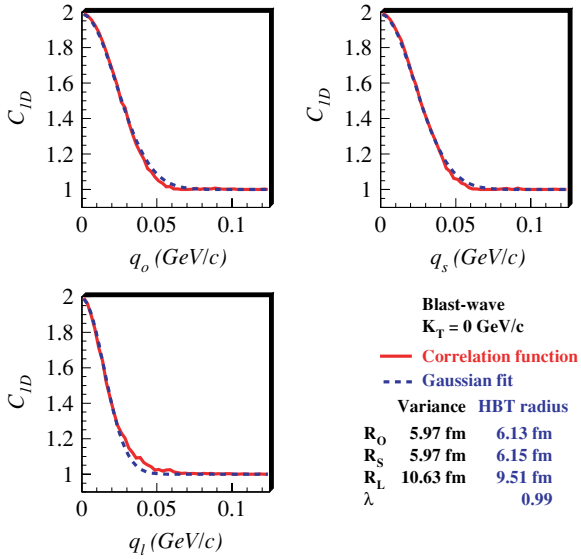

FIG. 1. (Color online) One-dimensional slices of the three-dimensional correlation function along the out, side, and long directions, for pion pairs with $\boldsymbol{K} = 0$, calculated from the blast-wave parametrization. For a given slice, the unplotted q components equal 1.25 MeV/c (i.e., the center of the first bin). The solid (red) curve is the calculated correlation function from Eq. (3), the dashed (blue) curve shows the same slice of the best 3D Gaussian fit (5), with HBT parameters calculated from the analytic expressions given in Sec. III B.

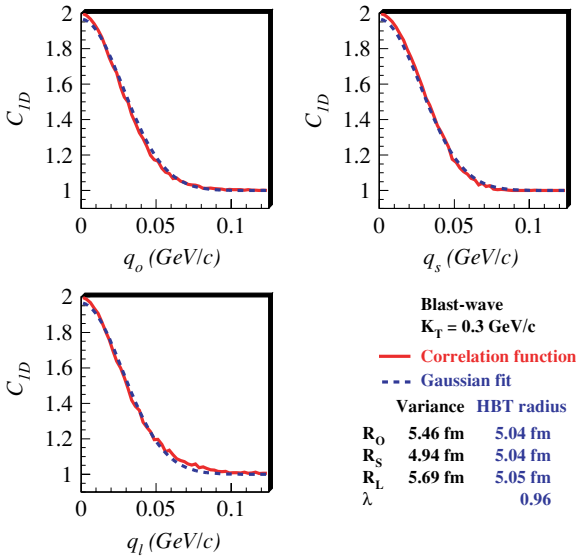

FIG. 2. (Color online) Solid (red) curves show one-dimensional slices of the three-dimensional correlation function calculated with Eq. (3) from the blast-wave parametrization, for midrapidity pions with $K_T = 0.3$ GeV/c. Dashed (blue) curves show slices of the three-dimensional Gaussian form of Eq. (5), with HBT parameters calculated from the analytic expressions given in Sec. III B.

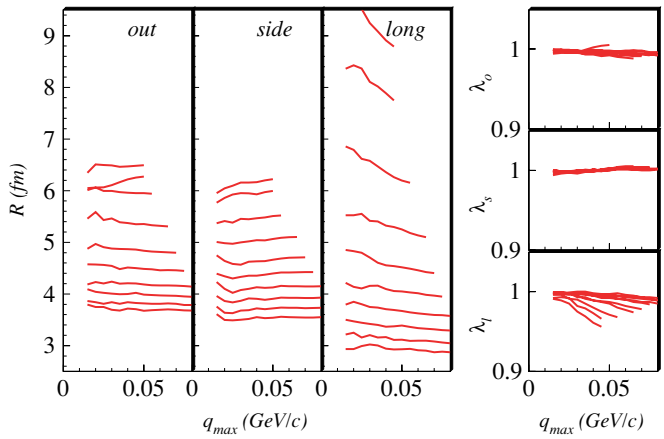

FIG. 3. (Color online) From the blast-wave parametrization, one-dimensional HBT fit parameters $R_{1D,i}$ and $\lambda_{1D,i}$ are calculated with Eqs. (13) and (14) and plotted as a function of the maximum allowed value of any q component; see text for details. Each curve corresponds to one of ten values of K_T: 0.0, 0.1, 0.2, . . . , 0.9 GeV/c. Curves corresponding to high K_T are at low (high) values of $R_{1D,i}$ ($\lambda_{1D,i}$).

of data points used. We study this sensitivity to the fit range in the following subsection.

B. Fit-range study

Since no measured correlation function is ever perfectly Gaussian, experimentalists typically perform so-called fit range studies. Here, the measured correlation function is fitted with the Gaussian form (5), using data points in a restricted range of $\boldsymbol{q}$. With correlation functions in the one-dimensional quantity $Q_{\rm inv}$ it is common to study the variation of fit parameters as the first few (lowest-$Q_{\rm inv}$) data points are left out of the fit. This is because statistical fluctuations in these

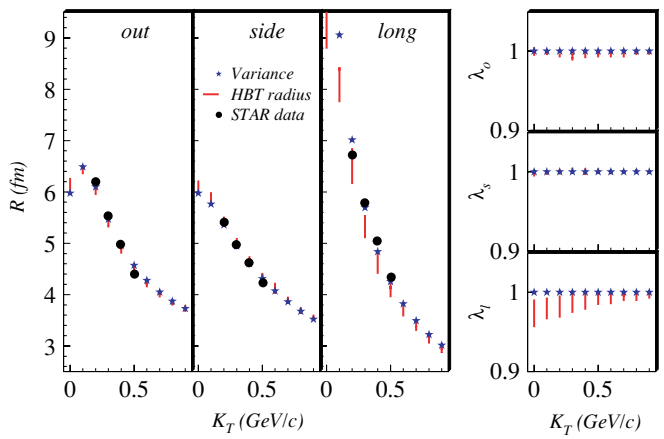

FIG. 4. (Color online) One-dimensional HBT fit parameters $R_{1D,i}$ and $\lambda_{1D,i}$ as a function of K_T, calculated from the blast-wave parametrization with Eqs. (13) and (14). For a given K_T, the vertical red line represents the variation with fit range (see Fig. 3). Blue stars represent the corresponding radius parameters calculated from the RMS variances by using Eqs. (6). Black circles show STAR data [4], with error bars removed for clarity.

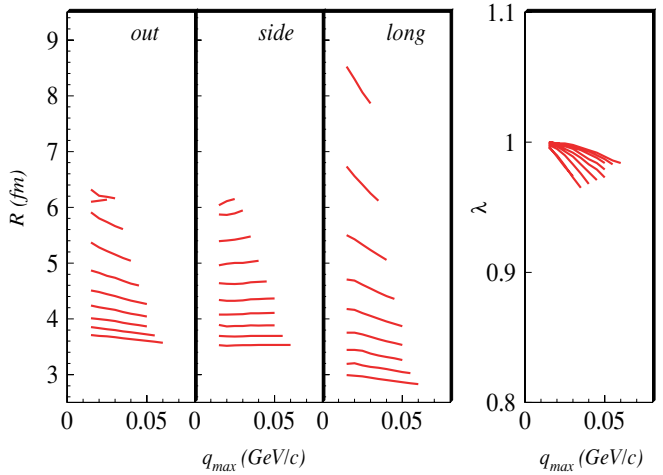

FIG. 5. (Color online) From the blast-wave parametrization, three-dimensional HBT fit parameters R_i and λ are calculated with Eqs. (21) and plotted as a function of the maximum allowed value of any q component; see text for details. Each curve corresponds to one of ten values of K_T: 0.0, 0.1, 0.2, . . . , 0.9 GeV/c. Curves corresponding to high K_T are at low (high) values of R_i (λ). The R_l curve for $K_T = 0$ falls above the plotting range.

bins may be quite large and may be due to the visible non-Gaussian nature of the measured correlation function there. Three-dimensional correlation functions do not suffer from these issues, and so usually the experimentalist includes all data points with $|q_i| < q_{\rm max}$ and studies variations of the fit parameters as $q_{\rm max}$ is varied; any such variations are typically folded into systematic errors on the HBT radii.

Here, we follow the experimentalists' approach. Using the correlation function generated from the blast-wave model, we

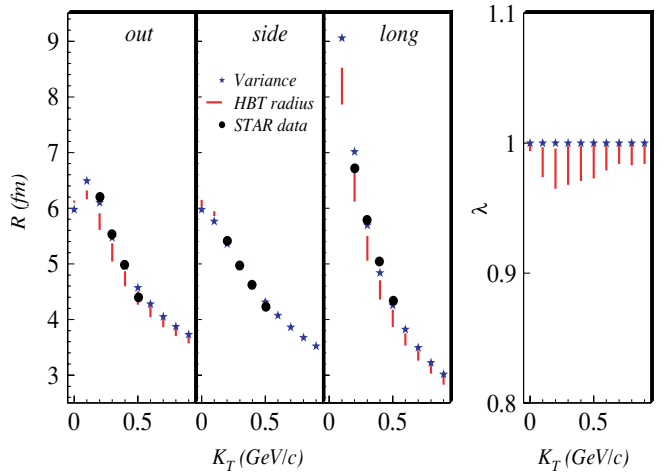

FIG. 6. (Color online) Three-dimensional HBT fit parameters $R_{1D,i}$ and $\lambda_{1D,i}$ as a function of K_T, calculated from the blast-wave parametrization with Eqs. (21). For a given K_T, the vertical red line represents the variation with fit range (see Fig. 5). Blue stars represent the corresponding radius parameters calculated from the RMS variances using Eqs. (6). Black circles show STAR data [4], with error bars removed for clarity.

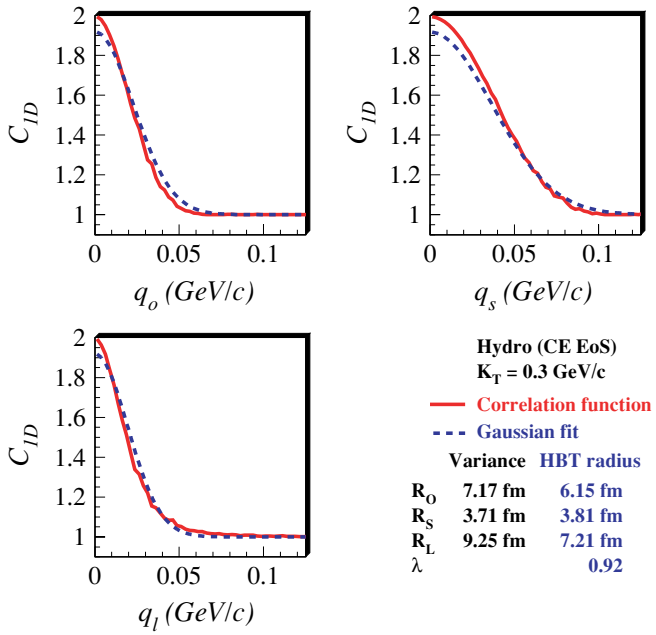

FIG. 7. (Color online) Solid (red) curves show one-dimensional slices of the three-dimensional correlation function calculated with Eq. (3) from the hydrodynamic model with the CE Equation of State, for midrapidity pions with $K_T = 0.3$ GeV/c. Dashed (blue) curves show slices of the three-dimensional Gaussian form of Eq. (5), with HBT parameters calculated from the analytic expressions given in Secs. III B.

calculate HBT parameters from 1D and 3D Gaussian fits as discussed in Secs. III A and III B, restricting the k sums in Eqs. (15), (16), (24), and (25) to include only those data points where all three q components have magnitudes less than $q_{\max}$ [27]. Thus, we will not calculate unique HBT radii, but a finite range for each fit parameter.

For various values of K_T, Fig. 3 shows the evolution of the 1D radii with $q_{\max}$. Except for R_l at low K_T, the parameter variation with fit range is quite mild, corresponding to a small non-Gaussian systematic error on the radii. In Fig. 4 the range of this variation, indicated by vertical lines, is plotted as a function of K_T. Consistent with the theorem [8] that the spatial RMS variances (6) of the source control the *curvature* of the correlator $C(\boldsymbol{q})$ at $\boldsymbol{q} = 0$, the blue stars in Fig. 4 coincide with the $q_{\max} \to 0$ limit of the fitted 1D radii. The largest fit-range variations, indicating the biggest non-Gaussian effects in the correlator, are seen at small pair momentum K_T. The fit-range sensitivity is most pronounced for R_l (where at low K_T it can exceed 0.5 fm) but almost negligible for R_o and R_s. In short, the 1D Gaussian fits to the two transverse projections of the correlation function give length scales consistent with the spatial RMS variances of the source distribution, but non-Gaussian features along the longitudinal projection cause the RMS variances to overestimate the longitudinal 1D HBT radius R_l by up to 0.5 fm at low K_T if a reasonable fit range $q_{\max}$ is used to extract the latter. This discrepancy is significantly larger than the combined statistical and systematic error on the experimental value for R_l [4].

Figures 5 and 6 show the same study for the three-dimensional Gaussian fits. For reasons explained in Sec. III, the non-Gaussian effects in a unified 3D Gaussian fit are expected to differ from those in 1D fits. Indeed, in the unified 3D fit non-Gaussian influences also appear in R_o, and both R_o and R_l now show fit-range variations that exceed the combined statistical and systematic errors of the data [4]. The largest fit-range sensitivity is still seen in the longitudinal direction. In Ref. [23] the blast-wave model parameters were determined by comparing RMS variances with the measured HBT radii (see Figs. 4 and 6), using the experimental errors on the latter to extract error estimates for the model parameters. The results presented here suggest that if the authors had instead compared the measured data with HBT radii extracted from a 3D Gaussian fit to the calculated correlation function, they would have found somewhat different model parameters whose mean values in some cases might even have fallen outside the likely parameter range quoted in Table II of Ref. [23]. In particular, such an apples-to-apples comparison may allow for somewhat larger fireball lifetimes τ and/or emission durations $\Delta\tau$ than quoted in Ref. [23]. While such an improved blast-wave model fit is numerically expensive and outside the scope of the present paper, it may be a worthwhile future project.

V. HBT RADII FROM HYDRODYNAMICS

Nonviscous (ideal) hydrodynamical calculations have successfully reproduced differential momentum spectra (at least perpendicular to the beam direction) at RHIC, including their anisotropies in noncentral collisions and the dependence of these anisotropies on the masses of the emitted hadrons [9]. As in the blast-wave model calculations, very strong collective flow is a critical ingredient to reproduce the data. (Of course, in the blast-wave parametrization such flow is put in by hand, while it arises naturally in the hydrodynamical model.)

Most (but not all [11–13,15,16]) hydrodynamic predictions of HBT radius parameters have been based on calculations of the spatial RMS variances from the hydrodynamically generated emission function, using Eqs. (6) [9,10]. In spite of the hydrodynamic model's impressive success in describing hadron spectra, these predictions of HBT radii were a failure: The calculated longitudinal radii R_l were too large (although this problem was less severe in Hirano and Tsuda's work [15]), while the predicted sideward radius R_s was too small, and both R_s and R_o showed much less dependence on K_T in theory than seen in the data. This, together with similar failures by other dynamical models (see [1] for a review), has become known as the RHIC HBT Puzzle.

Various possibilities to explain and correct this failure have been suggested. They include a more realistic modeling of the final freeze-out stage [28], exploration of fluctuations in the initial state and ambiguities in the hydrodynamic decoupling criterion [29], viscous effects due to incomplete thermalization (i.e., inapplicability of ideal fluid dynamics) [30], different (more Landau-type) initial conditions leading to strong longitudinal hydrodynamic acceleration [31], and the use of more realistic or different equations of state (EoS) for the expanding matter [32]. None of these suggestions,

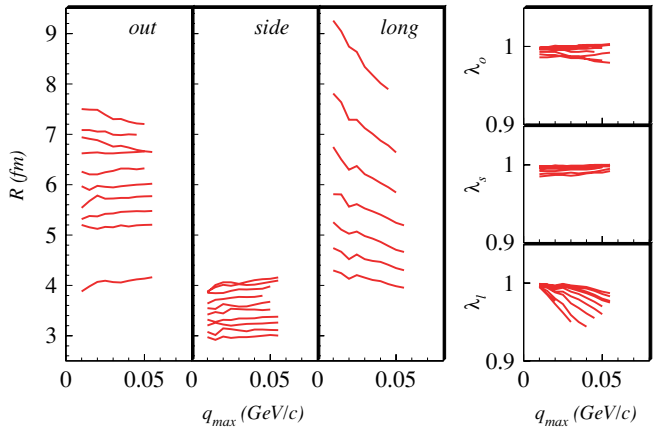

FIG. 8. (Color online) From the hydrodynamic model with CE EoS, one-dimensional HBT fit parameters $R_{1D,i}$ and $\lambda_{1D,i}$ are calculated with Eqs. (13) and (14) and plotted as a function of the maximum allowed value of any q component; see text for details. Each curve corresponds to one of ten values of K_T: 0.0, 0.1, 0.2, . . . , 0.9 GeV/c. Curves corresponding to high K_T are at low (high) values of $R_{1D,i}$ ($\lambda_{1D,i}$). The R_l curves for $K_T \leqslant 0.2$ GeV/c fall above the plotting range.

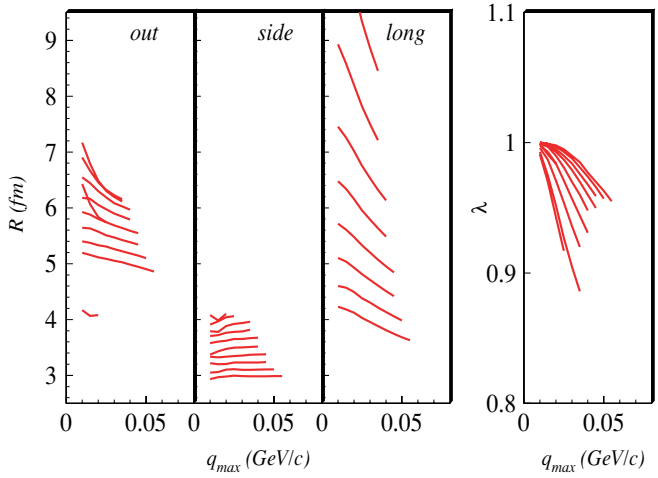

FIG. 10. (Color online) From the hydrodynamic model with CE EoS, three-dimensional HBT fit parameters R_i and λ are calculated with Eq. (21) and plotted as a function of the maximum allowed value of any q component; see text for details. Each curve corresponds to one of ten values of K_T: 0.0, 0.1, 0.2, . . . , 0.9 GeV/c. Curves corresponding to high K_T are at low (high) values of R_i (λ). The R_l curves for $K_T \leqslant 0.1$ GeV/c fall above the plotting range.

individually or in combination, has been convincingly shown to be able to solve the HBT puzzle. Motivated by the blast-wave study in the preceding section, we therefore explore here one further possibility: that previous comparisons of the data with hydrodynamic models might have been misleading, since the RMS variances from hydrogenerated sources differ significantly from HBT radii extracted from a Gaussian parametrization of the correlation function. Indications that this is indeed the case have already emerged from the work on 1D projections of Hirano and Tsuda [15] and Kolb [14], and with our new analytic 3D Gaussian fit algorithm we can improve on their analysis and study this question in more detail.

For our study of HBT radii from the hydrodynamic model we use two different sets of emission functions, obtained from running the hydrodynamic code with two different equations of state (EoS). Both EoS describe the quark-gluon plasma (QGP) as a free gas of massless particles, but they differ in their treatment of the late hadronic stage when the fireball has cooled below the critical temperature $T_c \approx 165$ MeV for hadronization. The CE EoS [33,34] assumes that the hadron resonance gas remains not only in thermal, but also in

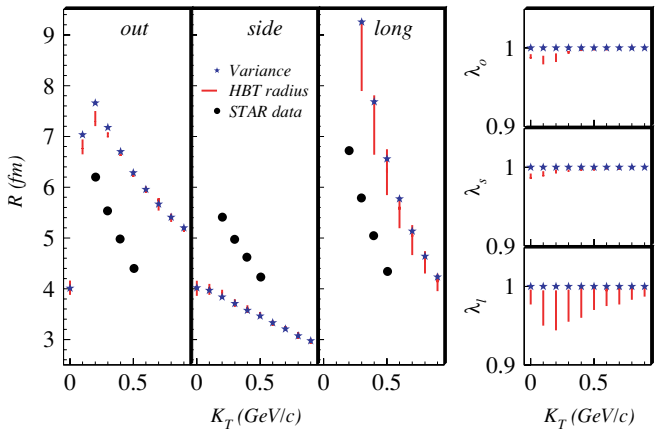

FIG. 9. (Color online) One-dimensional HBT fit parameters $R_{1D,i}$ and $\lambda_{1D,i}$ as a function of K_T, calculated from the hydrodynamic model using CE EoS with Eqs. (13) and (14)). For a given K_T, the vertical red line represents the variation with fit range (see Figure 8). Blue stars represent the corresponding radius parameters calculated from the RMS variances using Eq. (6). Black circles show STAR data [4], with error bars removed for clarity.

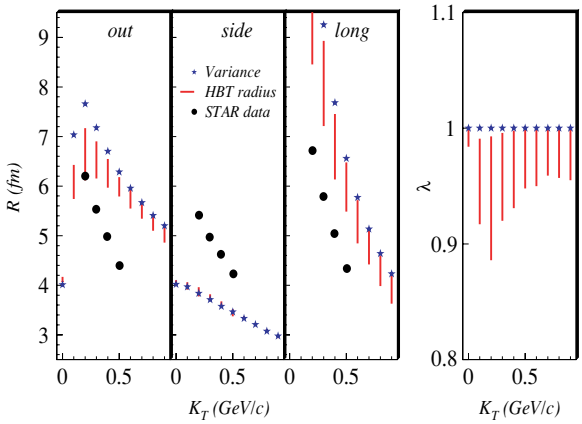

FIG. 11. (Color online) Three-dimensional HBT fit parameters $R_{1D,i}$ and $\lambda_{1D,i}$ as a function of K_T, calculated from the hydrodynamic model using CE EoS with Eq. (21). For a given K_T, the vertical red line represents the variation with fit range (see Fig. 10). Blue stars represent the corresponding radius parameters calculated from the RMS variances using Eqs. (6). Black circles show STAR data [4], with error bars removed for clarity.

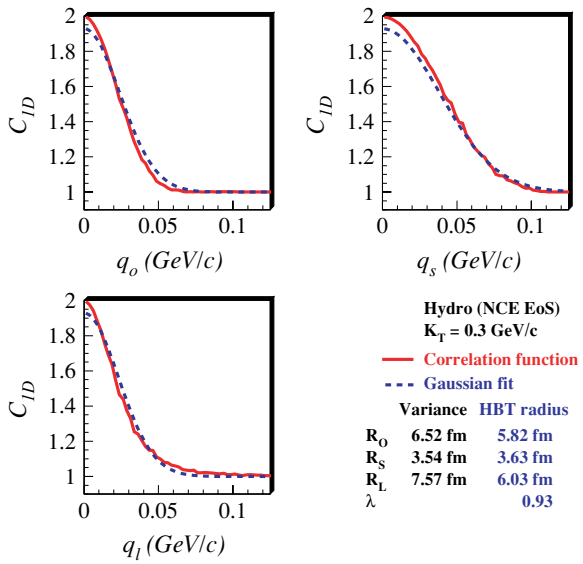

FIG. 12. (Color online) Solid (red) curves show one-dimensional slices of the three-dimensional correlation function calculated with Eq. (3) from the hydrodynamic model with the NCE EoS, for midrapidity pions with $K_T = 0.3$ GeV/c. Dashed (blue) curves show slices of the three-dimensional Gaussian form of Eq. (5), with HBT parameters calculated from the analytic expressions given in Sec. III B.

chemical equilibrium until final kinetic freeze-out. This fails to reproduce the observed hadron yields, which correspond to chemical equilibrium at a temperature of about 170 MeV [35]. The NCE EoS [15,36,37] takes the immediate decoupling of hadron abundances at T_c into account by introducing *nonequilibrium chemical* potentials for each hadron species, which ensure that the particle yields are held fixed as the temperature and density continue to decrease. While the CE EoS was used for the hydrodynamic model predictions made for RHIC before the accelerator turned on and the hadron abundances were measured, the NCE EoS is more realistic and has been used in most hydrodynamic studies since 2002. We here explore emission functions obtained with either EoS.

Figures 7–11 present 1D projections and 1D and 3D fit results, analogous to those from the previous section, for the emission function from hydrodynamic calculations using the CE EoS. Figures 12–16 show the same for the NCE EoS. Several observations are in order.

As is apparent from Figs. 7 and 12, the best 3D Gaussian fits do not fully reproduce the correlation function, even though the correlation function projections themselves appear rather Gaussian. Clearly, aspects of the correlation function not apparent in the one-dimensional projections are partially driving the 3D fit. Further, it is interesting to note that, while the projections in the side direction appear the worst reproduced by the fit, the greatest discrepancy between RMS variances and HBT radii are in fact in the out and long directions (c.f. Figs. 11 and 16). Both of these points emphasize that the three-dimensional correlator can contain important information that does not appear in its one-dimensional projections and thus in the one-dimensional fits. Particularly important in this case are strong non-Gaussian features in the longitudinal direction, which cause a significant suppression of the correlation strength parameter λ of the 3D Gaussian fit. This in turn creates the appearance of a bad fit in the sideward direction even though the 1D sideward projection looks quite Gaussian itself.

One draws the same conclusion by examining the fit-range systematics. As mentioned, non-Gaussian effects generate a variation of the HBT parameters with $q_{\max}$. As seen in Figs. 8 and 13, fits in the out and side directions produce 1D radii and directional λ_i parameters that vary very little with $q_{\max}$; strong fit-range sensitivity is only seen in the long direction, where the 1D projection deviates most strongly from a Gaussian form. In the three-dimensional fits, on the other hand (c.f. Figs. 10 and 15), the strong non-Gaussian features in the q_l direction now affect all four fit parameters, generating strong fit-range sensitivities for R_o and λ also.

There may (and in general will) be other properties of the three-dimensional correlation function to which the 1D projections and their Gaussian fits are not sensitive but that affect the 3D Gaussian fit. The extracted values for R_o and R_s thus in general depend significantly on the detailed conditions under which the Gaussian fit is performed. Hence, a meaningful and accurate comparison between models and experimental data requires that the Gaussian fit to the theoretical correlation functions be done under similar conditions and constraints (e.g., fit range) as in the experiment.

VI. DISCUSSION AND CONCLUSIONS

Let us close with some general observations and summarize our conclusions.

Except inasmuch as it couples HBT radii in a 3D fit, we have not focused here on the λ parameter, since comparison to measurements of λ is significantly complicated by experimental artifacts [1]. This is also the reason why tests of consistency between different experiments generally compare HBT radii, not λ. In all of the idealized calculations presented in this report, $C(|\boldsymbol{q}| = 0) = 2$, a purely Gaussian correlation function (generated by a purely Gaussian source) would yield $\lambda = 1$, with no fit-range systematics. Indeed, we find that $\lim_{q_{\max}\to 0} \lambda = 1$ (see, e.g., Fig. 10) as expected, but that its value declines as more bins are included in the fit. In experimental data, several factors cause λ to fall below its nominal value of unity. Our calculations confirm the generally held folklore that non-Gaussian effects may be important to understanding λ.

Of more fundamental interest are the characteristic length scales of the emission region. We have seen that RMS variances of model-calculated source functions, which are frequently compared with experimentally extracted HBT radii, may systematically differ from fitted HBT radii that characterize the shape of the correlation function from the same model. Since the latter quantity provides the best apples-to-apples comparison with published experimental data, this can be an important observation.

Previous attempts [14,15,21] to estimate the effect in hydrodynamical calculations have focused on numerical fits

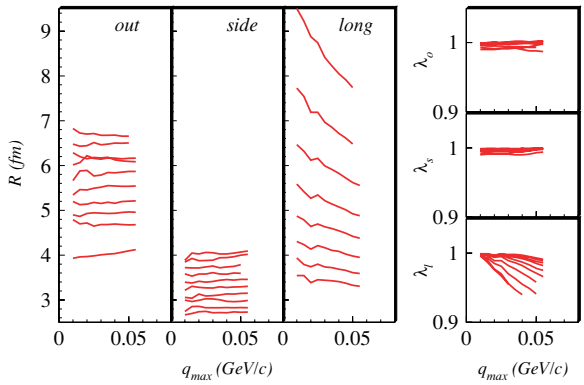

FIG. 13. (Color online) From the hydro model with NCE EoS, one-dimensional HBT fit parameters $R_{1D,i}$ and $\lambda_{1D,i}$ are calculated with Eqs. (13) and (14) and plotted as a function of the maximum allowed value of any q component; see text for details. Each curve corresponds to one of ten values of K_T: 0.0, 0.1, 0.2, . . . , 0.9 GeV/c. Curves corresponding to high K_T are at low (high) values of $R_{1D,i}$ ($\lambda_{1D,i}$). The R_l curves for $K_T \leqslant 0.1$ GeV/c fall above the plotting range.

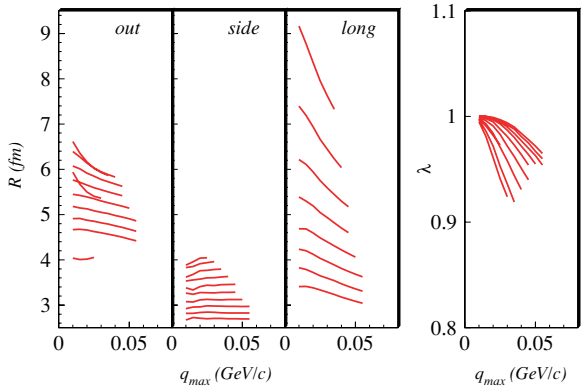

FIG. 15. (Color online) From the hydrodynamic model with NCE EoS, three-dimensional HBT fit parameters R_i and λ are calculated with Eqs. (21) and plotted as a function of the maximum allowed value of any q component; see text for details. Each curve corresponds to one of ten values of K_T: 0.0, 0.1, 0.2, . . . , 0.9 GeV/c. Curves corresponding to high K_T are at low (high) values of R_i (λ). The R_l curves for $K_T \leqslant 0.1$ GeV/c fall above the plotting range.

to several one-dimensional projections of the calculated correlation function. We here presented an analytic method to extract these 1D HBT radii from the projections and further generalized it to the full three-dimensional case. The 1D projections represent a set of zero measures of the full three-dimensional correlation function and, as we have seen, may not be sensitive to important three-dimensional information. This information influences the unified three-dimensional fit to the correlation function. Since the unified 3D fit most closely mimics the procedure of experimentalists, these effects are relevant for comparisons between models and data.

The magnitude of these effects are model dependent. The non-Gaussian nature of emission regions in the blast-wave parametrization has been noted before [23]. It was shown here to generate only minor deviations from Gaussian behavior in the transverse projections of the correlation function, but the longitudinal projection shows significant non-Gaussian features. In a unified 3D Gaussian fit, non-Gaussian features were seen to generate fit-range sensitivities for all four fit-parameters, leading to significant downward shifts of both R_l and R_o, especially at low K_T, relative to predictions based on the spatial RMS variances of the blast-wave source.

These tendencies were found to be even more strongly exhibited by the HBT radii extracted from hydrodynamic model sources. The differences between HBT radii extracted from 3D Gaussian fits of the correlator and the values (6)

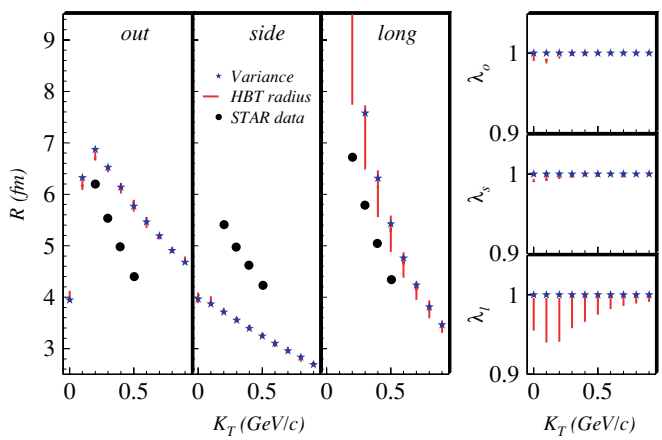

FIG. 14. (Color online) One-dimensional HBT fit parameters $R_{1D,i}$ and $\lambda_{1D,i}$ as a function of K_T, calculated from the hydrodynamic model using NCE EoS with Eqs. (13) and (14). For a given K_T, the vertical red line represents the variation with fit range (see Fig. 13). Blue stars represent the corresponding radius parameters calculated from the RMS variances using Eqs. (6). Black circles show STAR data [4], with error bars removed for clarity.

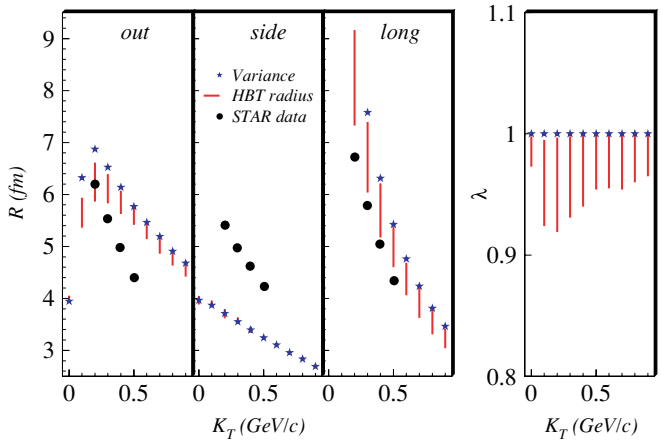

FIG. 16. (Color online) Three-dimensional HBT fit parameters $R_{1D,i}$ and $\lambda_{1D,i}$ as a function of K_T, calculated from the hydrodynamic model using NCE EoS with Eqs. (21). For a given K_T, the vertical red line represents the variation with fit range (see Figure 15). Blue stars represent the corresponding radius parameters calculated from the RMS variances using Eq. (6). Black circles show STAR data [4], with error bars removed for clarity.

calculated from the spatial RMS variances are quite significant and thus relevant in considerations of the RHIC HBT puzzle. In particular, for both equations of state considered here, the HBT radii in the out and long directions are significantly lower (and closer to the data) than the corresponding RMS variances that have been the basis of many puzzle discussions (c.f. Figs. 11 and 16). As in the blast-wave model, these 3D Gaussian fit effects seem to be driven mostly by strong non-Gaussian features in the longitudinal projection of the correlator. Combining improvements of using the NCE EoS and the use of HBT radii instead of RMS variances brings the hydrodynamic calculations for the longitudinal radius R_l into fair agreement with the data over the entire measured K_T range. A significant improvement is also seen in the outward direction, but it is concentrated mostly at low K_T, and hence the disagreement between the rather steep K_T dependence of the measured R_o radii and the much flatter K_T dependence of the theoretical results is becoming worse. The fitted sideward radii R_s show practically no deviation from the corresponding RMS variances, and the well-known [10] problem that the hydrodynamically predicted values are significantly smaller and show much less K_T dependence than the data is not alleviated by our improved comparison between theory and data.

While the results presented here cannot offer a resolution of all aspects of the RHIC HBT Puzzle, they refocus our perception of where the most severe problems are located. The strong non-Gaussian effects in the q_l direction and the resulting large downward shift of the fitted longitudinal radii (as compared with the corresponding RMS variances) largely eliminate the discrepancies between hydrodynamically predicted and measured R_l values. A number of authors have interpreted the smallness of the measured R_l values as evidence for a short fireball lifetime $\tau_f < 10$ fm/c, inconsistent with the O(15 fm/c) lifetimes predicted [9] by the hydrodynamic model. The analysis presented here resolves this problem. On the other hand, even when using the properly extracted Gaussian fit values for R_s and R_o and after taking into account the resulting decrease of R_o at low K_T, the theoretically predicted ratio R_o/R_s is still significantly larger than 1 over the entire measured K_T interval, in contradiction to the data. Furthermore, the decline of both R_o and R_s with increasing pair momentum is still much too weak in the model, in spite of the large transverse flow generated by the hydrodynamic expansion. These aspects of the HBT Puzzle remain serious and must be addressed by other theoretical improvements.

Finally, one should remember that the raw experimental correlation functions hardly ever appear very Gaussian, due to additional distortions by the final state Coulomb interactions between the two charged particles. Modern methods of extracting the HBT radii from the measured correlator include these Coulomb effects self-consistently in the fit function [1], leading to more complicated (numerical) fit algorithms than the analytical one presented in Sec. III. Nonetheless, the measured HBT radii extracted from such self-consistent 3D fits are affected by non-Gaussian structures in the underlying Bose-Einstein correlations in much the same way as discussed here for the simpler case of noninteracting particles. Thus, while Coulomb interactions should be included in future studies, our analysis should provide a good estimate of the direction and magnitude of non-Gaussian effects in blast-wave and hydrodynamical models, and it points out the importance of such effects in the comparison of theory to experiment.

ACKNOWLEDGMENTS

This work was supported by the U.S. National Science Foundation, grant PHY-0355007, and by the U.S. Department of Energy, grant DE-FG02-01ER41190.

[1] M. A. Lisa, S. Pratt, R. Soltz, and U. Wiedemann, Annu. Rev. Nucl. Part. Sci. **55**, 357 (2005) [arXiv:nucl-ex/0505014].
[2] S. V. Akkelin and Y. M. Sinyukov, Phys. Lett. **B356**, 525 (1995).
[3] U. A. Wiedemann and U. Heinz, Phys. Rev. C **56**, R610 (1997) [arXiv:nucl-th/9610043].
[4] J. Adams *et al*. (STAR Collaboration), Phys. Rev. C **71**, 044906 (2005) [arXiv:nucl-ex/0411036].
[5] D. A. Brown and P. Danielewicz, Phys. Lett. **B398**, 252 (1997) [arXiv:nucl-th/9701010].
[6] D. A. Brown, P. Danielewicz, M. Heffner, and R. Soltz, Acta Phys. Hung. A **24**, 111 (2005) [arXiv:nucl-th/0404067].
[7] D. A. Brown, A. Enokizono, M. Heffner, R. Soltz, P. Danielewicz, and S. Pratt, Phys. Rev. C **72**, 054902 (2005) [arXiv:nucl-th/0507015].
[8] U. A. Wiedemann and U. Heinz, Phys. Rep. **319**, 145 (1999) [arXiv:nucl-th/9901094].
[9] P. F. Kolb and U. Heinz, in *Quark-Gluon Plasma 3*, edited by R. C. Hwa and X.-N. Wang (World Scientific, Singapore, 2004), p. 634 [arXiv:nucl-th/0305084].
[10] U. Heinz and P. F. Kolb, in *Proceedings of the 18th Winter Workshop on Nuclear Dynamics*, edited by R. Bellwied, J. Harris, and W. Bauer (EP Systema, Debrecen, Hungary, 2002), p. 205 [arXiv:hep-ph/0204061].
[11] T. Hirano, K. Morita, S. Muroya, and C. Nonaka, Phys. Rev. C **65**, 061902(R) (2002) [arXiv:nucl-th/0110009].
[12] K. Morita, S. Muroya, C. Nonaka, and T. Hirano, Phys. Rev. C **66**, 054904 (2002) [arXiv:nucl-th/0205040].
[13] K. Morita and S. Muroya, Prog. Theor. Phys. **111**, 93 (2004) [arXiv:nucl-th/0307026].
[14] P. F. Kolb (private communication), May 2002.
[15] T. Hirano and K. Tsuda, Phys. Rev. C **66**, 054905 (2002) [arXiv:nucl-th/0205043].
[16] S. Bernard, D. H. Rischke, J. A. Maruhn, and W. Greiner, Nucl. Phys. **A625**, 473 (1997) [arXiv:nucl-th/9703017].
[17] D. Molnar and M. Gyulassy, Phys. Rev. Lett. **92**, 052301 (2004) [arXiv:nucl-th/0211017].
[18] D. Hardtke and S. A. Voloshin, Phys. Rev. C **61**, 024905 (2000) [arXiv:nucl-th/9906033].
[19] S. Soff, S. A. Bass, D. H. Hardtke, and S. Y. Panitkin, Phys. Rev. Lett. **88**, 072301 (2002) [arXiv:nucl-th/0109055].
[20] Z. w. Lin, C. M. Ko, and S. Pal, Phys. Rev. Lett. **89**, 152301 (2002) [arXiv:nucl-th/0204054].

[21] U. A. Wiedemann and U. Heinz, Phys. Rev. C **56**, 3265 (1997) [arXiv:nucl-th/9611031].
[22] A. Kisiel, W. Florkowski, W. Broniowski, and J. Pluta, arXiv:nucl-th/0602039.
[23] F. Retiere and M. A. Lisa, Phys. Rev. C **70**, 044907 (2004) [arXiv:nucl-th/0312024].
[24] S. Pratt, Phys. Rev. Lett. **53**, 1219 (1984).
[25] Note that for one-dimensional correlations measured in $Q_{\rm inv} = \sqrt{-q^\mu q_\mu}$, as opposed to one-dimensional slices of the three-dimensional correlator, phase-space considerations usually produce larger uncertainties at small $Q_{\rm inv}$.
[26] U. Heinz, A. Hummel, M. A. Lisa, and U. A. Wiedemann, Phys. Rev. C **66**, 044903 (2002) [arXiv:nucl-th/0207003].
[27] When the HBT radii are large (e.g., at low K_T), the correlator approaches unity quickly with increasing $|\boldsymbol{q}|$, and the quantity $\ln[C(\boldsymbol{q}^{(k)}) - 1]$ becomes numerically unwieldy; in these cases only small values of $q_{\rm max}$ are used.
[28] S. Soff, S. A. Bass, and A. Dumitru, Phys. Rev. Lett. **86**, 3981 (2001) [arXiv:nucl-th/0012085].
[29] O. Socolowski Jr., F. Grassi, Y. Hama, and T. Kodama, Phys. Rev. Lett. **93**, 182301 (2004) [arXiv:hep-ph/0405181].
[30] D. Teaney, Phys. Rev. C **68**, 034913 (2003).
[31] T. Renk, Phys. Rev. C **70**, 021903(R) (2004) [arXiv:hep-ph/0404140].
[32] P. Huovinen, Nucl. Phys. **A761**, 296 (2005) [arXiv:nucl-th/0505036].
[33] J. Sollfrank, P. Huovinen, M. Kataja, P. V. Ruuskanen, M. Prakash, and R. Venugopalan, Phys. Rev. C **55**, 392 (1997) [arXiv:nucl-th/9607029].
[34] P. F. Kolb, J. Sollfrank, and U. Heinz, Phys. Rev. C **62**, 054909 (2000) [arXiv:hep-ph/0006129].
[35] P. Braun-Munzinger, D. Magestro, K. Redlich, and J. Stachel, Phys. Lett. **B518**, 41 (2001) [arXiv:hep-ph/0105229].
[36] P. F. Kolb and R. Rapp, Phys. Rev. C **67**, 044903 (2003) [arXiv:hep-ph/0210222].
[37] D. Teaney, arXiv:nucl-th/0204023.